J Mater Sci (2007) 42:6541–6548
DOI 10.1007/s10853-007-1523-z

Flow through an evolving porous media—compressed foam

D. A. Graf von der Schulenburg · M. Paterson-Beedle · L. E. Macaskie · L. F. Gladden · M. L. Johns

Received: 4 August 2006 / Accepted: 16 January 2007 / Published online: 30 April 2007

Abstract Magnetic Resonance Imaging (MRI) techniques were applied such that they were able to provide simultaneously both 3D pore-scale velocity and microstructural data for polyurethane foam with water flowing through it. This necessitated the use of velocity gating of the relevant images in order to describe accurately the position of the solid foam walls; a pore thinning algorithm was used to differentiate individual pores within the foam pore space where minima in hydraulic radius defined pore boundaries. This methodology was then used to explore the effect of foam compression on both pore geometric characteristics and pore-scale velocity fields. Pore volumes were seen to decrease from 3.27 to 0.96 mm^3 as porosity was reduced from 0.84 to 0.61 and increased flow channelling, adjacent to the containing cylinder, was observed. The velocity fields were compared with corresponding Lattice Boltzmann flow simulations with good agreement being produced.

Introduction

Flow through porous media is fundamental to a number of industrial processes ranging from oil recovery from rocks to the use of packed beds for catalytic reactions. Until relatively recently, the hydrodynamics of such systems were typically studied on the macroscopic scale via measurement of pressure drop, superficial velocity and tracer dispersion [1]. However a number of examples of tomographic techniques being used to image hydrodynamics in porous media on a pore-scale have appeared in the literature; these include the use of Magnetic Resonance Imaging (MRI) [e.g. 2–4]. MRI allows the in-situ, spatially resolved measurement of flow velocities, diffusion, dispersion and mass transfer in the porous medium. A particularly powerful use of this spatially resolved data is the stringent verification of simulations of the pore-scale hydrodynamics, including the Lattice Boltzmann (LB) technique [e.g. 5–7], which has been demonstrated to be particularly suited to describe flow and mass transfer in such complex geometries. Such simulations can then be used to relate macroscopic characteristics to pore-scale events and provide a thorough understanding of their origin.

Foamed solids are a form of porous media characterised by high porosities and typically geometrically complex pore space. They are used in a variety of industrial applications ranging from thermal isolation and filters to carrier materials for lubricants or enzymes [8]. The polyurethane foam considered in this study is used as a support material for bioreactor applications [e.g. 9, 10]; thus flow through the pore space is an essential aspect of its use. Applications of imaging techniques to foam have generally focussed on their microstructure characteristics (local porosity, pore volume, pore diameter and wall thickness) which usually dictate their functionality [11]. These include the application of MRI [12, 13] to image the pore space of foam filled with water or direct imaging of the solid foam material using X-ray tomography [e.g. 14, 15].

In the current study we apply standard 3D MRI velocimetry to image simultaneously both the microstructure and the local pore-scale velocity distribution inside

D. A. G. von der Schulenburg · L. F. Gladden · M. L. Johns (✉)
Department of Chemical Engineering, University of Cambridge, Pembroke Street, Cambridge CB2 3RA, UK
e-mail: mlj21@cam.ac.uk

M. Paterson-Beedle · L. E. Macaskie
School of Bioscience, University of Birmingham, Edgbaston, Birmingham B15 2TT, UK

polyurethane foam; this is performed as a function of in-situ foam compression. To enable the microstructural characterisation, a 3D structural image of the pore space is required. Methods to generate this in-situ using MRI were considered. The 3D structural image produced was subsequently used for simulations of the pore-scale flow fields through the foam using LB techniques, the results of which are compared directly to the corresponding experimental velocimetry data. The pore space of the foam structure image was further portioned according to a pore-partitioning algorithm [16], which identifies pore boundaries as minima in hydraulic radius. The change in pore volume, surface area, free surface area and pore connectivity were all quantified as a function of the compression extent.

In summary the aims of the work presented here are thus:

- To enable simultaneous 3D microstructure and velocity imaging of foam using MRI.
- To explore how these velocity fields and microstructural characteristics change in response to foam compression.
- To use the velocity and microstructural data to verify a LB simulation of the flow field through the foam.

To the best of our knowledge we report the first pore-scale imaging and simulation of hydrodynamics through foam and subsequently the first detailed analysis of the effect of compression on both the pore structure and hydrodynamics.

Methodology

Materials

The foam consisted of 1 cm^3 polyurethane reticulated foam cubes (Recticel, Belgium), several of these were placed on top of one another in a 1 cm diameter cylindrical glass flow cell, up to an initial height of 10 cm. The foam cubes were thus slightly larger than the glass flow cell to prevent initial flow channelling adjacent to the wall. As will be shown in Fig. 5, the resultant compression of the cubes required to insert them into the tube produced an approximately homogeneous porosity distribution across the cubes. A schematic of the cell is shown in Fig. 1; two exit ports at the top and one port at the bottom allowed water to be pumped through the foam sample. The cell was placed inside the NMR spectrometer magnet and water was pumped through it at a constant flow rate of 5 ml/min. The top of the cell had a moveable plug which allowed for variable axial compression of the foam content. The plug head had a conical shape with a cone height of 3 mm. This could be done in-situ in the spectrometer magnet. The bulk

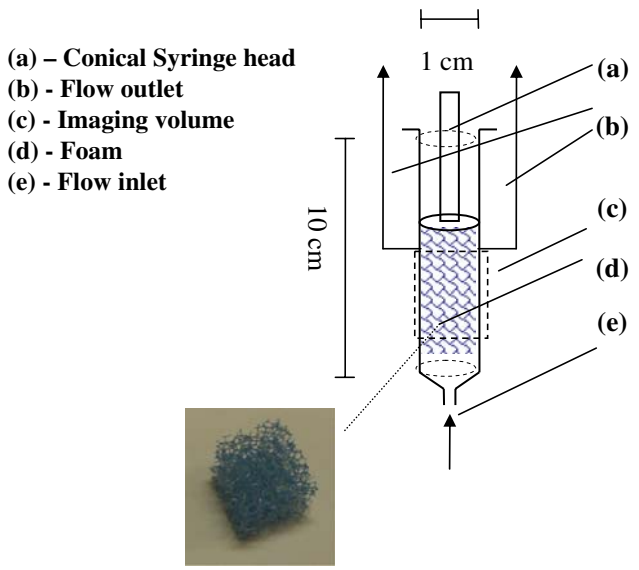

Fig. 1 Schematic of the flow cell used. A photograph of a foam cube is also included

porosity (ε) of the original foam was 0.86 (determined gravimetrically). Velocity and microstructure imaging was performed at three levels of compression resulting in porosities of: $\varepsilon_1 = 0.84$, $\varepsilon_2 = 0.82$ and $\varepsilon_3 = 0.61$, hereafter referred to as compression levels 1, 2 and 3.

MRI

All measurements were acquired using a Bruker 400 MHz vertical magnet with a 2 cm inner diameter radio-frequency coil for ^1H resonance, which was used exclusively. A standard 3D spin echo pulse sequence was used to image the water within the foam and a 3D phase shift velocity encoding pulse sequence was used for corresponding velocimetry. A detailed treatment of relevant MRI can be found in [17], further details of the pulse sequences used are contained in [2]. All imaging was performed over a field of view of $40 \times 20 \times 20$ mm^3 (40 mm in flow direction), resulting in an isotropic resolution of 156 μm, the position of this imaging volume is shown in Fig. 1. For phase shift velocity encoding, a gradient increment, ΔG, of 2.9 G/cm was used, which avoided fold-over artefacts.

X-ray imaging

An X-ray image of the dry foam was used to determine the average thickness of the foam walls. This was acquired using a desktop Skyscan 1072 Microtomograph apparatus with an isotropic resolution of 18.32 μm for a rectangular region of size $1024 \times 1024 \times 512$ pixels. Image reconstruction was performed using Cone-Rec software (Skyscan, Belgium).

Pore partitioning algorithm

For the microstructural analysis of the resultant MRI foam images, a pore partioning algorithm was used, which has successfully been applied to other forms of porous media including bead packs and rock cores [e.g. 16]. The algorithm defines a pore as being a discrete portion of the total pore space bounded by the solid matrix and planes between pores where the hydraulic radius of the pore space is a local minimum (referred to as a pore neck). Having portioned the pore space into individual pores using this algorithm, pore statistics can then be computed to characterise the microstructure of the particular system; these include pore volume, surface area, radius, coordination number (number of neighbouring pores) and free surface area (i.e. that connected to other pores).

Lattice Boltzmann method

The lattice Boltzmann (LB) method was used to simulate the pore scale flow field through the foam. Describing the dynamics of fluids in complex pore structures becomes extremely difficult on a microscopic or molecular level. The LB method models the hydrodynamics of fluids on a mesoscopic level by simulating probability distribution functions for the fluid particles $f_i(\vec{x},t)$ on a discrete lattice $\vec{x}$ in a discrete evolution time t. The evolution of $f_i(\vec{x},t)$ is governed by the Lattice Bhatnagar-Gross-Krook (LGBK) equation:

$$f_i(\vec{x}+\vec{c},t+1)-f_i(\vec{x},t)=-\frac{1}{\tau}(f_i(\vec{x},t)-f_i^{eq}(\vec{x},t)), \qquad (1)$$

where $\vec{c}_i$ is the velocity for each lattice direction i (i = 1,2,3…19) and τ is the Bhatnagar-Gross-Krook [18] relaxation parameter. $f_i^{eq}(\vec{x},t)$ is the equilibrium distribution function given by [19]:

$$f_i^{eq}(\rho,\vec{u};\vec{x},t)=\rho A_i+\overline{\rho}\left(B_i\vec{c}_i\vec{u}+C_i\vec{c}_i^2\vec{u}^2+D_iu^2\right) \qquad (2)$$

where $\vec{u}$ is the local lattice velocity and ρ is the local particle density. Appropriate expansion of Eq. 2 enables continuity and the Navier Stokes equation to be recovered by selection of the constant coefficients A_i, B_i, C_i and D_i [18, 20]. Via this expansion, τ is related to the lattice viscosity of the fluid, v, by:

$$v=\frac{1}{3}\left(\tau-\frac{1}{2}\right). \qquad (3)$$

$\vec{u}$ and ρ are calculated for each lattice site by the following summations:

$$\rho=\sum_i f_i(\vec{x},t), \qquad (4)$$

and

$$\overline{\rho}\vec{u}=\sum_i f_i(\vec{x},t)\times c_i. \qquad (5)$$

In our study a non-slip boundary condition at the fluid-solid interface is implemented as a halfway bounce-back boundary condition [21]. Our LB method has been applied to a variety of different 'fluid flow through complex geometries' scenarios and shown excellent agreement with both experimental results and analytical solutions [5, 6, 22, 23]. The method is second–order accurate and computationally inexpensive [21]. All calculations are done with double floating point precision.

The lattice Boltzmann method used in the current work was applied to the various foam images over a volume of $128 \times 128 \times 47$ pixels^3, with an isotopic resolution of

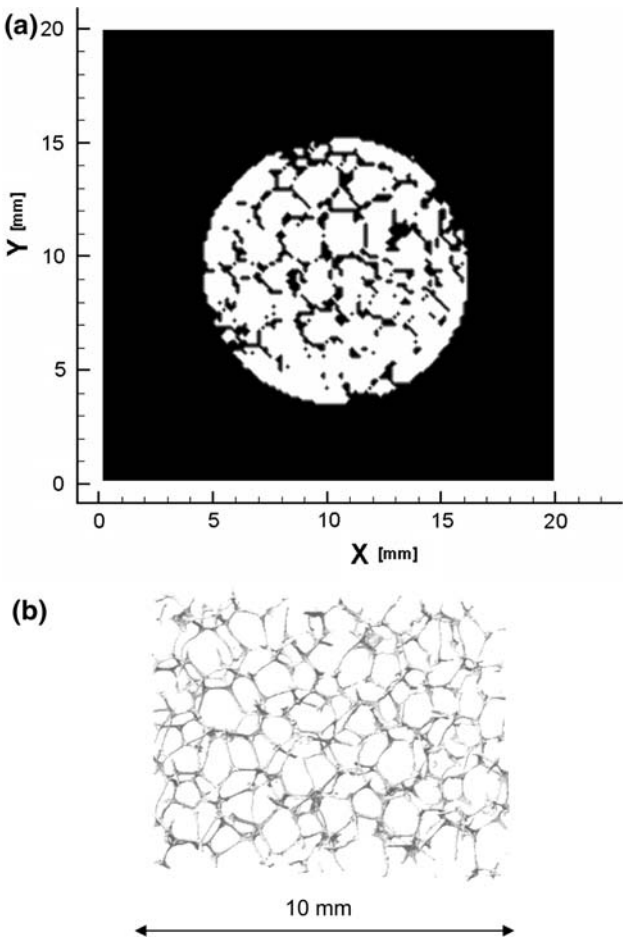

Fig. 2 (**a**) The projection of 7 x–y MRI slices into the axial (z) direction for the gated velocity data. (**b**) A rendered 3D X-ray microtomography image of a single foam cube

156 μm. The relaxation parameter τ was set to 0.99 and the LB simulations were run until steady state (relative error between iterations $<10^{-8}$).

Results and discussion

Generation of microstructure lattice

Simple MRI of the water within the foam structures was unable to resolve adequately the internal microstructure of the foam. X-ray imaging of a dry foam sample revealed that the foam walls varied in thickness from approximately 36–90 μm. Given that the imaging resolution of the MRI is 156 μm, the lack of adequate definition of the internal foam walls is thus to be expected as the voxels in the vicinity of the foam wall will only be partially filled with water. It would be possible to perform the imaging at a higher resolution, but this would be prohibitive in terms of acquisition time or sample size able to be accommodated.

Hence, in order to resolve the foam structure, the following procedure was applied. The full 3 component velocity image (examples of which will follow shortly) was converted into a speed image. The resultant image was then binary gated such that speed values below a certain threshold were assigned to be foam walls and the rest assigned to be pore space; the threshold value was selected such that the known value of foam porosity was produced. The assumption is that the foam structure has no 'dead zones' and that virtually stagnant flow is only encountered adjacent to the solid foam walls. Given the high porosity of the foam structure (0.86), this assumption seems to be appropriate. The resultant 3D image of the foam microstructure is presented in Fig. 2a as the projection of 7 2D slices in the axial direction. The X-ray image of the foam before compression is also shown in Fig. 2b. Figure 2a and

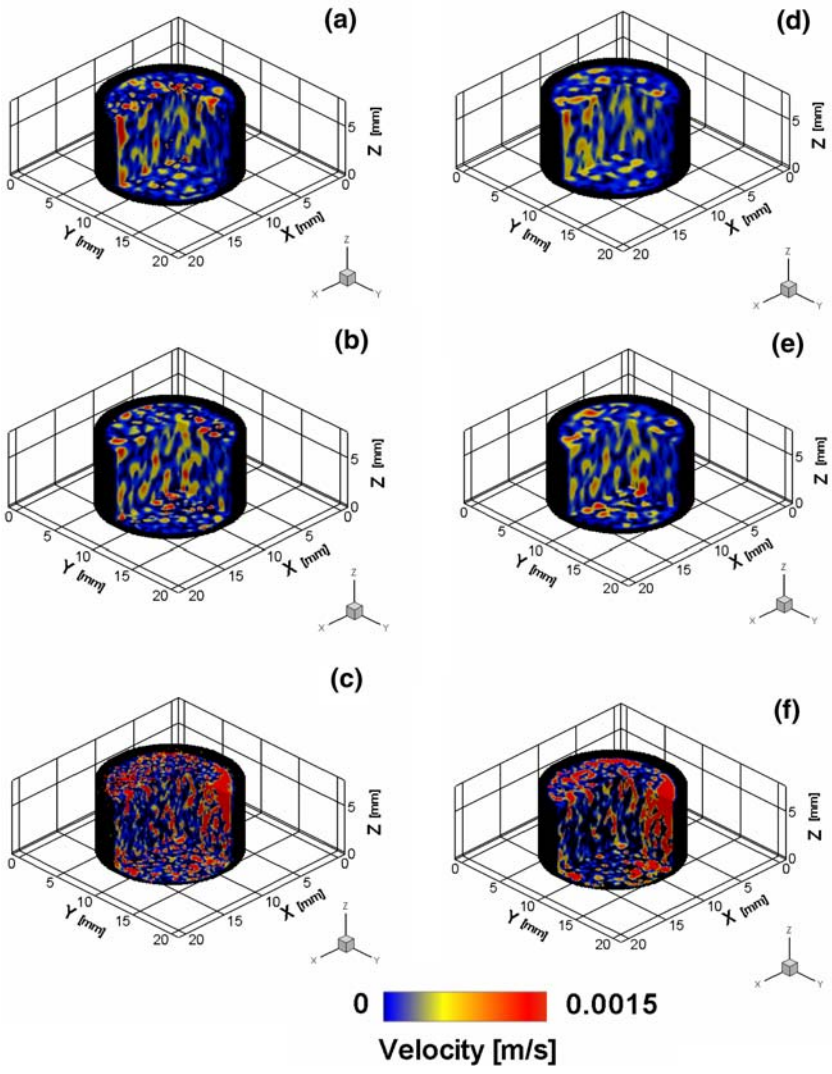

Fig. 3 3D Velocity images for the first (**a**), second (**b**) and third (**c**) compression levels and the corresponding lattice Boltzmann simulations: (**d**), (**e**) and (**f**) respectively. The superficial flow is in the positive z direction

b suggest that an adequate microstructural image of the foam with polygonal pores has been produced; this statement will be further clarified when we consider pore characteristics and the ability of the LB simulations to re-create the pore-scale hydrodynamics. This velocity gating method was subsequently used to produce all foam microstructure MRI images and hence LB simulation lattices.

Comparison of compression extents and experimental data with LB simulations

The velocity field images for compression levels 1–3 ($\varepsilon_1 = 0.84$, $\varepsilon_2 = 0.82$ and $\varepsilon_3 = 0.63$) are shown in Fig. 3a–c respectively. The mean pore-scale velocity in the axial superficial flow direction for the three compression levels were u_z (ε_1) = 3.70×10^{-4} m/s, u_z (ε_2) = 3.72×10^{-4} m/s and u_z (ε_3) = 6.41×10^{-4} m/s, as expected these velocities increased with decreasing porosity. There is a general increase in flow heterogeneity as the foam is compressed. The simulated LB flow fields for the three corresponding compression stages are shown in Fig. 3d–f respectively; the simulation lattices having been generated using the procedure outlined previously. There is reasonable agreement between the LB simulations and the corresponding MRI data for all compression stages. To quantify this difference, histograms of voxel velocity in the axial superficial flow direction are presented in Fig. 4a–c respectively, also included are the corresponding histograms from a matrix subtraction of the LB simulation result and the corresponding MRI data. The difference histograms are all centred on zero and their widths are considerably narrower than the true distribution. This supports the use of the gating procedure to provide an adequate microstructural representation. The agreement is poorer for the highest compression level (ε_3) suggesting that our assumption of no stagnant zones might be slightly compromised in this case.

Figure 5a shows the radial axial velocity profile for the three compression levels. A radial position of 0 corresponds to the centre of the sample; the various velocities presented are then the mean velocity at the radial distance from the centre. As expected the velocity at the wall is 0 for all three compression stages. An increase in velocity is most evident in Fig. 5a for compression level 3 at a radial position of approximately 4 mm. This is a consequence of the foam folding inwards as compression is applied allowing comparatively large gaps to develop adjacent to the foam walls; some flow channelling thus occurs, as seen clearly in both the MRI images and the LB simulations (Fig. 3). We believe that this response to the compression is induced by the conical shape of the punch which introduces in-homogenous strain [24] and thus the observed radial porosity and velocity inhomogeneities. Figure 5b shows the corresponding radial porosity profiles for compression stages 1–3, as determined from the simulation lattices. Compression levels 1 and 2 show no radial variation in porosity, however compression level 3 shows a linear increase in porosity with radial position. This results in an increase in axial velocity (Fig. 5a) with radial position, although there is not a direct correlation between

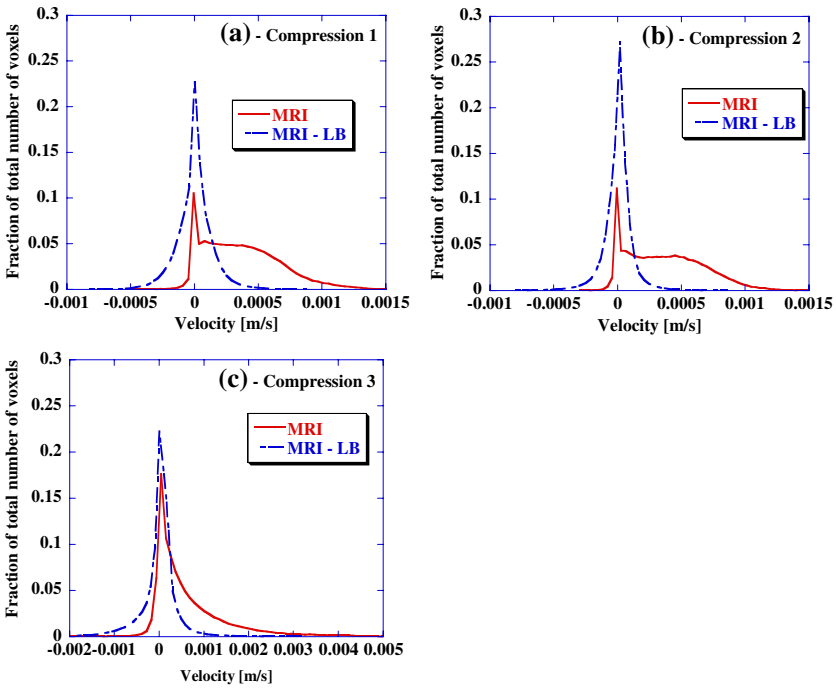

Fig. 4 MRI Velocity histogram and histogram of the absolute difference between MRI velocity images and LB simulations for the compression levels: one (**a**), two (**b**) and three (**c**)

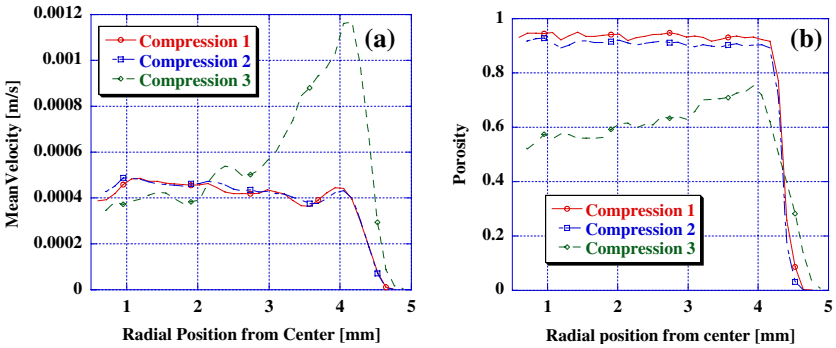

Fig. 5 Radial velocity (**a**) and porosity (**b**) profile for the three compression levels

porosity and velocity. Figure 6a–c shows how these radial velocity profiles compare with the corresponding LB data—these are in very good agreement for all three compression levels.

Structural analysis for the lattice images of the three compression levels based on the pore partitioning algorithm was then applied. Figure 7 shows the microstructure lattice, corresponding to compression level 1, after the application of the pore partitioning algorithm; different colours differentiate different pores. The change in the mean pore volume, mean pore area, mean coordination number, mean surface area connection ratio and number of pores over the three compression levels are presented in Table 1. Note that visual inspection with a micrometer of the internal surface foam suggested an approximate average pore diameter of 1.8 mm, which corresponds to a spherical pore volume of 3.05 mm^3, which is in excellent agreement with the corresponding value of 3.27 mm^3 for compression 1. Comparable pore dimensions of polyurethane foams were reported in the literature based on scanning electron micrograph (SEM) measurements [9]. The application of the pore partitioning algorithm to the X-ray image to extract pore statistics did not lead to sensible results, we believe due to either image noise or polymer surface roughness. Visual inspection of the pore space of the X-ray image suggested an average pore diameter of 1.9 mm, in agreement with the MRI results.

The surface area connection ratio is the fraction of the pore's surface area that is connected to other pores. The following trend can be observed from Table 1 for the compression of foams: compression induces an increase in the number of pores with both lower mean volumes and mean surface areas. It further induces a decrease in the connectivity between pores; a pore is on average connected to less other pores and has a lower fraction of its surface area connected to these pores. The phenomenon of an

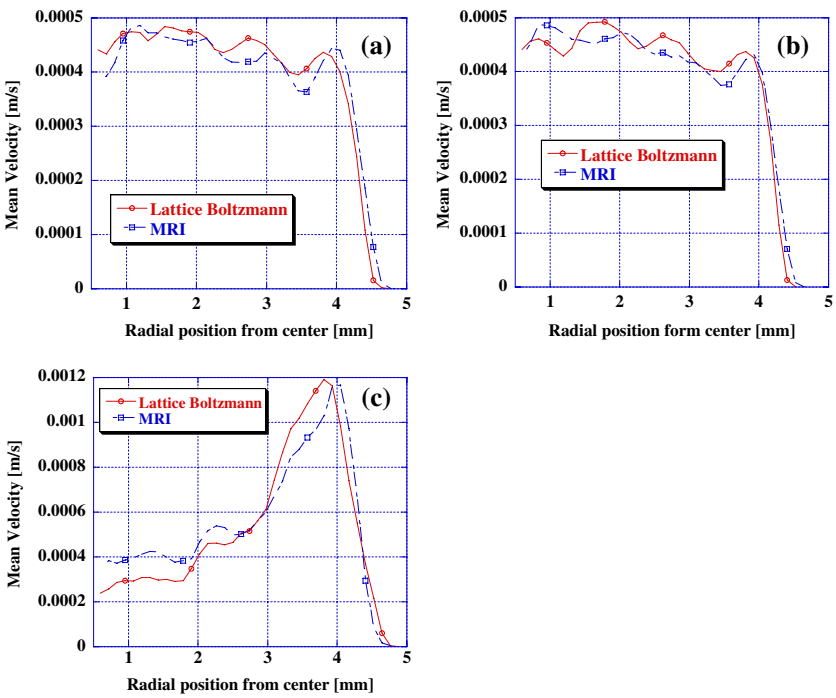

Fig. 6 Radial velocity profiles for comparison of lattice Boltzmann simulations and MR images for the three compression levels 1 (**a**), 2 (**b**) and 3 (**c**)

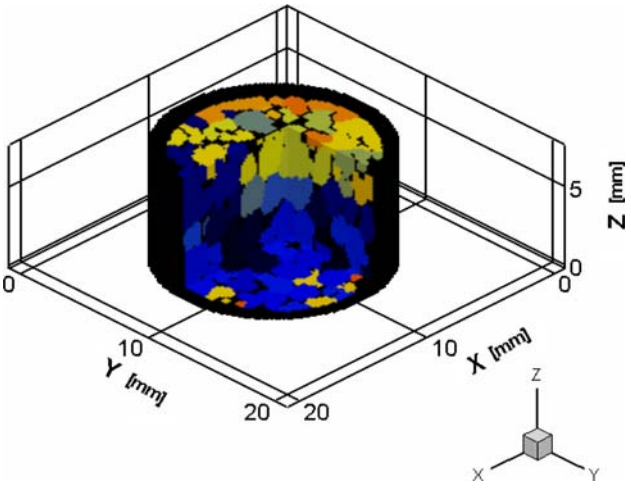

Fig. 7 The structural image after applying the pore partitioning algorithm. Different pores are shown by different colours

increasing pore number is related to the compression behaviour of the foam: foam under compression folds the same number of foam walls into a smaller volume, which devides this volume into more pores. This explains the decrease in mean pore volume and mean pore area as compression is increased.

Figure 8a and b show the number-based histograms for the pore volume and the pore surface area. As compression increases, there is a definite reduction in the number of larger pores and an increase in smaller pores. Figure 8c shows the histogram of the fraction of the pore surface area that is connected to other pores for the three compression stages. With an increasing compression the maxima of the surface area connection ratio distribution decreases which is compatible with the observed trend of a decrease in pore connectivity under compression.

Conclusion

3D pore-scale hydrodynamics through foam were successfully imaged using MRI. A method of simultaneously delivering microstructure characteristics was also presented. Both microstructure and velocity fields were quantified as a function of foam compression; mean pore volumes were seen to decrease and a more heterogeneous

Table 1 Pore statistics for the three compression levels

	Mean pore volume [mm^3]	Mean pore area [mm^2]	Mean pore coordination number	Mean surface area connection ratio	Number of pores
Compression 1	3.27	19.11	9.69	0.64	261
Compression 2	2.73	15.53	9.56	0.57	271
Compression 3	0.96	9.22	9.01	0.33	683

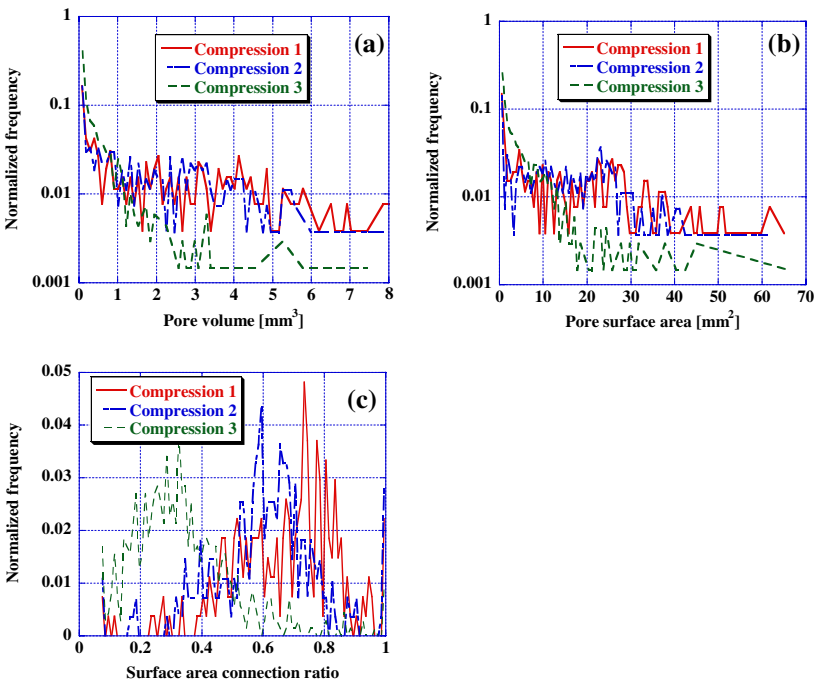

Fig. 8 Pore volume (**a**), pore surface area (**b**) and surface area connection ratio (**c**) number-based histograms for the three compression levels

flow profile was evident as compression was increased. The pore-scale hydrodynamics was adequately modelled using LB techniques. Future work will focus on extending this imaging (both structure and flow) and modelling platform to describe the development of biofilms within the foam structure and their subsequent use for ion exchange [9].

Acknowledgements The authors wish to acknowledge Dr. Peter R. Laity for acquiring the X-ray image of the foam, Reticel, Belgium for supplying the foam and the EPSRC for financial support.

References

1. Bear J (1972) In: Dynamics of fluids in porous media. Elsevier, New York
2. Sederman AJ, Johns ML, Bramley AS, Alexander P, Gladden LF (1997) Chem Eng Sci 52:2239
3. Sederman AJ, Johns ML, Alexander P, Gladden LF (1998) Chem Eng Sci 53:2117
4. Johns ML, Sederman AJ, Bramley AS, Gladden LF, Alexander P (2000) AIChE J 46:2151
5. Mantle MD, Sederman AJ, Gladden LF (2001) Chem Eng Sci 56:523
6. Mantle MD, Bijeljic B, Sederman AJ, Gladden LF (2001) MRI 19:527
7. Johns ML, Sederman AJ, Davis S, Wilson A, Gladden LF (2003) AIChE J 49:1076
8. Gibson LJ, Ashby MF (1988) In: Cellular solids. Cambridge University Press
9. Macaskie LE, Yong P, Paterson-Beedle M, Thackray AC, Marquis PM, Sammons RL, Nott KP, Hall LD (2005) J Biotechnol 118:187
10. Nott KP, Heese FP, Hall LD, Macaskie LE, Paterson-Beedle M (2005) AIChE J 51:3072
11. Weiare D, Hutzler S (1999) In: The physics of foam. Oxford University Press
12. Kose K (1996) J Magn Reson 118:195
13. Kashiwagi K, Kose K (1997) NMR Biomed 10:13
14. Saadatfar M, Arns CH, Knackstedt MA, Senden T (2004) Colliods Surf A 263:284
15. Viot P, Bernard D (2006) J Mater Sci 41:1277
16. Baldwin CA, Sederman AJ, Mantle MD, Alexander P, Gladden LF (1996) J Colloid Interf Sci 181:79
17. Callaghan PT (1991) Principles of nuclear magnetic resonance microscopy. Oxford Press, New York, p 420
18. Chen S, Doolen GD (1998) Annu Rev Fluid Mech 30:329
19. He X, Luo LS (1997) J Stat Phys 88:927
20. Wolfram S (1986) J Stat Phys 45:471
21. Gallivan MA, Noble DR, Georgiadis JG, Buckius RO (1997) Int J Numer Methods Fluids 25:249
22. Sullivan SP, Johns ML, Matthews SM, Fisher AC (2005b) Electrochem Commun 7:1323
23. Sullivan SP, Gladden LF, Johns ML (2006) J Non-Newtonian Fluid Mech 133:91
24. Viot P, Beani F, Lataillade J-L (2005) J Mater Sci 40:5829